

# The ALMA-QUARKS survey: Extensive detection of acetamide in multiple high-mass star-forming regions <sup>★</sup>

Chunguo Duan<sup>1,2</sup>, Xuefang Xu<sup>1,2</sup>, Qian Gou<sup>1,2</sup>, Tie Liu<sup>3,4</sup>, Laurent Pagani<sup>5</sup>, Fengwei Xu<sup>6,7</sup>, Ke Wang<sup>7</sup>, Xunchuan Liu<sup>3,4,8</sup>, Jun Kang<sup>1,2</sup>, Mingwei He<sup>1,2</sup>, Jiaxiang Jiao<sup>1,2</sup>

<sup>1</sup> School of Chemistry and Chemical Engineering, Chongqing University, Daxuecheng South Rd. 55, Chongqing 401331, People's Republic of China

<sup>2</sup> Chongqing Key Laboratory of Chemical Theory and Mechanism, Chongqing University, Daxuecheng South Rd. 55, Chongqing 401331, People's Republic of China

<sup>3</sup> Shanghai Astronomical Observatory, Chinese Academy of Sciences, Nandan Rd. 80, Shanghai 200030, People's Republic of China

<sup>4</sup> Key Laboratory for Research in Galaxies and Cosmology, Shanghai Astronomical Observatory, Chinese Academy of Sciences, Nandan Rd. 80, Shanghai 200030, People's Republic of China

<sup>5</sup> LUX, Observatoire de Paris, PSL Research University, CNRS, Sorbonne Universités, UPMC Univ. Paris 06, 75014 Paris, France

<sup>6</sup> Department of Astronomy, Peking University, 5 Yiheyuan Road, Haidian District, Beijing 100871, People's Republic of China

<sup>7</sup> Kavli Institute for Astronomy and Astrophysics, Peking University, 5 Yiheyuan Road, Haidian District, Beijing 100871, People's Republic of China

<sup>8</sup> Leiden Observatory, Leiden University, P.O. Box 9513, 2300RA Leiden, The Netherlands

September 3, 2025

## ABSTRACT

Acetamide ( $\text{CH}_3\text{CONH}_2$ ), a key interstellar amide and a methyl derivative of formamide ( $\text{NH}_2\text{CHO}$ ), has been sparsely detected, limiting insights into its prebiotic relevance. We present the first systematic survey for acetamide toward 52 hot molecular cores using ALMA Band 6 data. Acetamide has been detected in 10 cores, markedly expanding the inventory of known emitters. The derived column densities of acetamide range from  $(2.5 \pm 0.9) \times 10^{14}$  to  $(1.5 \pm 0.6) \times 10^{16} \text{ cm}^{-2}$ , compared to formamide's  $(1.1 \pm 0.1) \times 10^{15}$  to  $(6.9 \pm 0.4) \times 10^{16} \text{ cm}^{-2}$ . The nearly constant abundance ratios ( $\sim 3$ – $9$ ) and strong abundance correlation between the two amides across sources suggest a chemically linked formation pathway, likely on grain surfaces. The presence of peptide-like molecules in these regions implies that complex organic species can survive star formation processes, offering a potential pathway toward prebiotic chemistry. These findings constrain the dominant grain-surface formation routes of acetamide, confirm its broader prevalence in high-mass star-forming regions, and underscore the importance of targeted amide surveys in tracing the chemical evolution toward prebiotic complexity.

**Key words.** ISM: molecules – ISM: abundances – Astrochemistry

## 1. Introduction

Life on Earth appeared about 700 million years after planetary formation ( $\sim 3.8$  billion years ago; [Pearce et al. 2018](#)), yet the mechanisms driving its origin remain unknown. What is clear is that life depends on recurring chemical motifs. Among them, the amide functional group ( $-\text{NH}-\text{C}(\text{O})-$ ) is central to peptide bonds and essential for biochemistry ([Pauling et al. 1951](#)).

Understanding how amides appeared on early Earth is vital for tracing the chemical origin of life. While they may have formed through prebiotic processes on Earth ([Patel et al. 2015](#)), an alternative scenario involves their formation in space and subsequent delivery by meteorites or comets ([Chyba et al. 1990](#); [Chyba & Sagan 1992](#)). Such molecules could have originated in the interstellar medium (ISM), within the parental molecular cloud of the Solar System. This raises the possibility that

analogous prebiotic pathways operate in other planetary systems across the Milky Way.

To assess the prebiotic chemistry relevance of amides, it is crucial to determine their presence in star- and planet-forming regions. Formamide ( $\text{NH}_2\text{CHO}$ ), the simplest amide and a key prebiotic precursor, has been widely detected across various astrophysical environments (e.g., [Zheng et al. 2024](#); [Zeng et al. 2023](#); [Liu et al. 2022](#); [Ligterink et al. 2020](#), and the review by [López-Sepulcre et al. 2019](#) for a comprehensive list of observations). Recent observations further confirmed its prevalence in star forming regions ([Xu et al. 2025](#)). In contrast, acetamide ( $\text{CH}_3\text{CONH}_2$ ), a methylated derivative of formamide representing a potential step toward more complex biomolecules, has been detected in only a handful of star-forming regions, including Sgr B2 ([Hollis et al. 2006](#); [Halfen et al. 2011](#); [Belloche et al. 2017](#); [Zheng et al. 2024](#)), NGC 6334I ([Ligterink et al. 2020](#)), G31.41+0.31 ([Colzi et al. 2021](#)), and Orion KL ([Cernicharo et al. 2016](#)), as well as the intermediate-mass protostar Serpens SMM1-a ([Ligterink et al. 2022](#)) and the low-mass protostar IRAS 16293-2422B ([Ligterink et al. 2017](#)). Notably, no

<sup>★</sup> Corresponding authors:

Xuefang Xu, e-mail: [xuefang\\_xu@cqu.edu.cn](mailto:xuefang_xu@cqu.edu.cn)

Qian Gou, e-mail: [qian.gou@cqu.edu.cn](mailto:qian.gou@cqu.edu.cn)

Tie Liu, e-mail: [liutie@shao.ac.cn](mailto:liutie@shao.ac.cn)

**Table 1.** Parameters of HMCs sample.

ID	Sources name	R.A. (J2000)	decl. (J2000)	$V_{\text{LSR}}^{\text{a}}$ (km s <sup>-1</sup> )	$D_{\text{GC}}^{\text{b}}$ (kpc)	$^{12}\text{C}/^{13}\text{C}^{\text{c}}$
1	I08303	08:32:09.190	-43:13:44.30	14.5	9.0	63.7
2	I08470	08:48:47.720	-42:54:22.00	12.1	8.8	62.7
3	I09018	09:03:32.820	-48:28:06.20	9.9	8.8	62.7
4	I11298	11:32:06.030	-62:12:20.50	33.4	10.1	68.9
5	I12326	12:35:34.810	-63:02:32.10	-39.5	7.2	55.1
6	I13079	13:11:13.730	-62:34:40.20	-41.3	6.9	53.7
7	I13134	13:16:42.990	-62:58:29.30	-32.0	6.9	53.7
8	I13140	13:17:15.900	-62:42:27.00	-34.4	6.9	53.7
9	I13471	13:50:42.100	-61:35:14.90	-57.8	6.4	51.3
10	I13484	13:51:58.640	-61:15:43.30	-55.3	6.4	51.3
11	I14498	14:53:42.530	-59:08:53.20	-50.2	6.4	51.3
12	I15254	15:29:19.480	-56:31:23.20	-68.6	5.7	47.9
13	I15437	15:47:33.110	-53:52:43.90	-83.4	5.0	44.6
14	I15520	15:55:48.390	-52:43:09.80	-41.8	6.2	50.3
15	I16060	16:09:52.850	-51:54:54.70	-92.1	4.5	42.2
16	I16065	16:10:19.600	-52:06:07.10	-62.5	5.2	45.6
17	I16071	16:10:59.010	-51:50:21.60	-86.5	4.5	42.2
18	I16076	16:11:27.120	-51:41:56.90	-87.8	4.5	42.2
19	I16164	16:20:10.910	-50:53:15.50	-56.7	5.4	46.5
20	I16172	16:21:02.930	-50:35:11.60	-53.3	5.4	46.5
21	I16272	16:30:58.020	-48:43:46.60	-46.8	5.8	48.4
22	I16318	16:35:33.200	-47:31:11.30	-120.8	3.3	36.5
23	I16344	16:38:10.380	-47:04:56.70	-49.7	5.4	46.5
24	I16348	16:38:29.420	-47:00:39.70	-47.8	5.4	46.5
25	I16351	16:38:50.610	-47:27:59.70	-40.8	5.7	47.9
26	I16458	16:49:30.410	-45:17:53.60	-50.9	5.1	45.1
27	I16484	16:52:03.990	-46:08:24.60	-32.4	6.4	51.3
28	I16547	16:58:17.260	-42:52:04.50	-30.6	5.8	48.4
29	I17008	17:04:23.200	-40:44:24.90	-17.3	6.1	49.9
30	I17016	17:05:11.020	-41:29:07.80	-26.8	7.0	54.2
31	I17158	17:19:20.340	-39:03:53.30	-16.6	5.1	45.1
32	I17175 MM1	17:20:53.570	-35:46:59.80	-8.7	7.0	54.2
33	I17175 MM2	17:20:53.570	-35:46:59.80	-8.7	7.0	54.2
34	I17220	17:25:24.990	-36:12:41.10	-97.2	1.3	27.0
35	I17233	17:26:42.800	-36:09:16.80	-3.1	7.0	54.2
36	I17441	17:47:19.790	-28:23:05.70	50.8	0.2	21.7
37	I18032	18:06:14.300	-20:31:35.00	4.4	3.4	37.0
38	I18056	18:08:38.180	-19:51:49.00	66.4	1.6	28.4
39	I18089	18:11:51.060	-17:31:27.20	32.9	5.9	48.9
40	I18117	18:14:39.250	-17:51:59.80	37.1	5.9	48.9
41	I18159	18:18:54.340	-16:47:45.90	22.4	6.9	53.7
42	I18182	18:21:09.220	-14:31:46.80	59.3	4.1	40.3
43	I18236	18:26:25.650	-12:03:57.60	26.1	6.3	50.8
44	I18290	18:31:42.980	-09:22:26.00	84.0	4.0	39.8
45	I18316	18:34:20.580	-05:59:41.60	42.7	6.5	51.8
46	I18411	18:43:46.260	-03:35:23.90	103.5	4.0	39.8
47	I18469	18:49:33.150	-01:29:06.20	86.6	4.7	43.2
48	I18507+0110	18:53:18.120	+01:15:00.10	58.2	7.1	54.6
49	I18507+0121	18:53:18.150	+01:25:22.40	57.8	7.1	54.6
50	I18517	18:54:14.110	+04:41:43.10	43.9	6.6	52.2
51	I19078	19:10:13.410	+09:06:10.40	6.2	7.6	57.0
52	I19095	19:11:53.900	+09:35:45.90	43.8	5.8	48.4

**Notes.**<sup>a</sup> The  $V_{\text{LSR}}$  was retrieved from [Liu et al. \(2024\)](#).<sup>b</sup> The  $D_{\text{GC}}$  was retrieved from [Liu et al. \(2020\)](#).<sup>c</sup> The  $^{12}\text{C}/^{13}\text{C}$  ratio was derived from the formula proposed by [Yan et al. \(2023\)](#).

large-sample survey has yet confirmed widespread acetamide emission.

Expanding the number of amide detections is essential in order to evaluate its role in prebiotic chemistry. Although astrochemical models have incorporated potential reaction networks for formamide and acetamide ([Belloche et al. 2017, 2019; Gar-](#)

[rod et al. 2022](#)), observational constraints – especially for larger amides – remain sparse. To address this gap, we present the first systematic search for acetamide across 52 hot molecular cores (HMCs) using Band 6 observations from the Atacama Large Millimeter/submillimeter Array (ALMA). Our detections substantially increase the number of known acetamide sources, en-

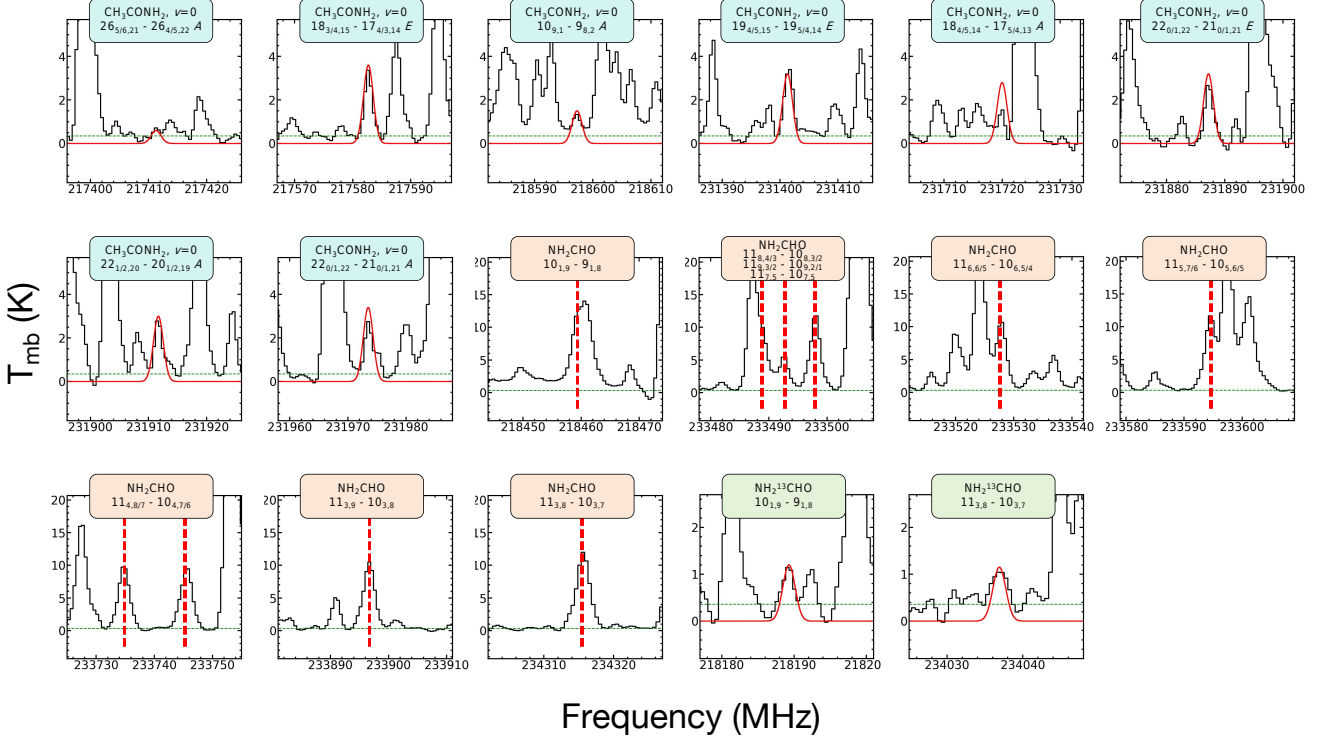


**Fig. 1.** Observed (black) and modeled (red) spectra of  $\text{CH}_3\text{CONH}_2$ ,  $\text{NH}_2\text{CHO}$ , and  $\text{NH}_2^{13}\text{CHO}$  in I17175 MM2. Clearly resolved or slightly blended transitions are shown. Green dashed lines mark the  $3\sigma$  noise level. No modeled spectrum is shown for  $\text{NH}_2\text{CHO}$  due to optical thickness. Red dashed lines indicate the rest frequencies of  $\text{NH}_2\text{CHO}$  transitions. Spectra for other sources are shown in Fig. B.1.

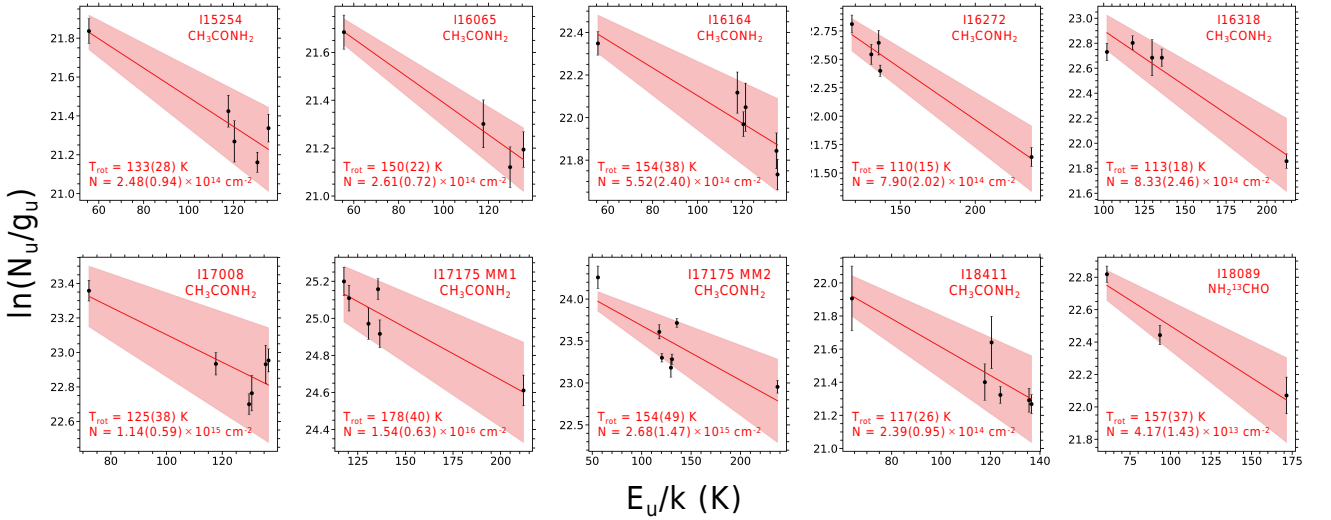


**Fig. 2.** Rotational diagrams of  $\text{CH}_3\text{CONH}_2$  and  $\text{NH}_2^{13}\text{CHO}$ . Black points represent the observed data, while red lines indicate the best-fit results. Shaded red regions denote the associated fitting uncertainties. Each panel includes the source name and molecule in the top-right corner, with the derived rotational temperature ( $T_{\text{rot}}$ ) and column density ( $N$ ) shown in the bottom-left.

abling a comparative analysis with formamide. These findings offer new insights into interstellar amide chemistry and its potential connection to prebiotic molecular evolution.

This paper is structured as follows. Sect. 2 outlines the source sample and the observational setup. Sect. 3 presents detection results and derivation of column densities, excitation temperatures. Sect. 4 discusses chemical correlations and formation pathways. Sect. 5 summarizes our conclusions.

## 2. Observations

This study is based on a sample of HMCs summarized in Table 1. The targets were selected from the QUARKS survey (Querying Underlying mechanisms of massive star formation with ALMA-Resolved gas Kinematics and Structures; Liu et al. 2024), based on HMC candidates previously identified by Qin et al. (2022). QUARKS is a 1.3 mm follow-up to the ALMA Three-millimeter Observations of Massive Star-forming Regions (ATOMS; Liu

**Table 2.** Parameters of detected amide molecules.

Source	$\theta_{\text{source}}$  (arcsec)	$\text{NH}_2^{13}\text{CHO}$				$\text{NH}_2\text{CHO}$				$\text{CH}_3\text{CONH}_2$				Ratio <sup>c</sup>	
		FTMW	$V_{\text{LSR}}$	$T_{\text{ex}}$	$N$	FTMW	$V_{\text{LSR}}$	$N$	$X_{\text{CH}_3\text{OH}}^b$	FTMW	$V_{\text{LSR}}$	$T_{\text{ex}}$	$N$		$X_{\text{CH}_3\text{OH}}^b$
		(km s <sup>-1</sup> )	(km s <sup>-1</sup> )	(K)	(cm <sup>-2</sup> )	(km s <sup>-1</sup> )	(km s <sup>-1</sup> )	(cm <sup>-2</sup> )		(km s <sup>-1</sup> )	(km s <sup>-1</sup> )	(K)	(cm <sup>-2</sup> )		
I15254	1.0	2.6	-66.6	133 <sup>a</sup>	(2.4±0.2)×10 <sup>13</sup>	2.7	-66.6	(1.1±0.1)×10 <sup>15</sup>	(6.3±0.7)×10 <sup>-4</sup>	3.4	-66.6	133±28	(2.5±0.9)×10 <sup>14</sup>	(1.4±0.5)×10 <sup>-4</sup>	4.6±1.8
I16065	2.9	2.7	-60.1	150 <sup>a</sup>	(4.2±0.3)×10 <sup>13</sup>	5.4	-59.5	(1.9±0.1)×10 <sup>15</sup>	(1.5±0.2)×10 <sup>-3</sup>	3.1	-59.5	150±22	(2.6±0.7)×10 <sup>14</sup>	(2.0±0.6)×10 <sup>-4</sup>	7.3±2.1
I16164	3.8	3.3	-59.7	157 <sup>a</sup>	(7.4±0.5)×10 <sup>13</sup>	5.3	-59.7	(3.5±0.2)×10 <sup>15</sup>	(3.8±0.3)×10 <sup>-3</sup>	2.8	-59.7	154±38	(5.5±2.4)×10 <sup>14</sup>	(6.1±2.6)×10 <sup>-4</sup>	6.2±2.7
I16272	1.4	2.8	-45.9	110 <sup>a</sup>	(1.2±0.2)×10 <sup>14</sup>	5.1	-46.3	(5.6±1.2)×10 <sup>15</sup>	(1.8±0.4)×10 <sup>-3</sup>	2.7	-46.3	110±15	(7.9±2.0)×10 <sup>14</sup>	(2.5±0.6)×10 <sup>-4</sup>	7.1±2.3
I16318	2.3	4.7	-118.2	113 <sup>a</sup>	(2.0±0.3)×10 <sup>14</sup>	7.7	-118.5	(7.4±1.0)×10 <sup>15</sup>	(2.7±0.4)×10 <sup>-3</sup>	3.6	-117.8	113±18	(8.3±2.5)×10 <sup>14</sup>	(3.0±0.9)×10 <sup>-4</sup>	8.9±2.9
I17008	1.3	4.4	-19.5	125 <sup>a</sup>	(1.4±0.3)×10 <sup>14</sup>	7.4	-19.1	(7.0±1.7)×10 <sup>15</sup>	(2.2±0.5)×10 <sup>-3</sup>	4.8	-19.8	125±38	(1.1±0.6)×10 <sup>15</sup>	(3.6±1.9)×10 <sup>-4</sup>	6.1±3.5
I17175 MM1	2.1	4.1	-5.1	178 <sup>a</sup>	(1.3±0.1)×10 <sup>15</sup>	7.3	-4.9	(6.9±0.4)×10 <sup>16</sup>	(1.1±0.1)×10 <sup>-2</sup>	4.4	-4.5	178±40	(1.5±0.6)×10 <sup>16</sup>	(2.4±1.0)×10 <sup>-3</sup>	4.5±1.9
I17175 MM2	1.6	3.8	-8.7	154 <sup>a</sup>	(1.51±0.01)×10 <sup>14</sup>	3.1	-8.7	(8.2±0.7)×10 <sup>15</sup>	(1.3±0.1)×10 <sup>-3</sup>	2.5	-8.7	154±49	(2.7±1.5)×10 <sup>15</sup>	(4.3±2.3)×10 <sup>-4</sup>	3.0±1.7
I18089	1.8	1.9	29.9	157±37	(4.2±1.4)×10 <sup>13</sup>	4.4	31.4	(2.0±0.7)×10 <sup>15</sup>	(7.9±2.7)×10 <sup>-4</sup>	4.1	29.9	157 <sup>a</sup>	(6.9±1.3)×10 <sup>14</sup>	(2.7±0.5)×10 <sup>-4</sup>	2.9±1.2
I18411	0.9	2.1	105.5	117 <sup>a</sup>	(3.0±0.3)×10 <sup>13</sup>	5.2	105.8	(1.2±0.1)×10 <sup>15</sup>	(1.3±0.1)×10 <sup>-3</sup>	2.2	105.5	117±26	(2.4±1.0)×10 <sup>14</sup>	(2.6±1.1)×10 <sup>-4</sup>	4.9±2.0

**Notes.**

<sup>a</sup> For  $\text{NH}_2^{13}\text{CHO}$ , excitation temperature fitting errors are not provided due to fewer than three clean transitions. Column densities are derived by assuming the excitation temperatures for  $\text{CH}_3\text{CONH}_2$ . For  $\text{CH}_3\text{CONH}_2$  in I18089, the column density is derived by assuming fixed excitation temperatures of  $\text{NH}_2^{13}\text{CHO}$ , due to the small energy range of the upper level for the three detected lines of  $\text{CH}_3\text{CONH}_2$ .

<sup>b</sup> Molecular abundances relative to  $\text{CH}_3\text{OH}$ , where  $\text{CH}_3\text{OH}$  column densities are adopted from [Qin et al. \(2022\)](#).

<sup>c</sup> Molecular ratios of  $\text{NH}_2\text{CHO}$  to  $\text{CH}_3\text{CONH}_2$ .

[et al. 2020](#)), aiming to resolve substructures within 3 mm core clusters in massive star-forming clumps ([Liu et al. 2020](#)).

The QUARKS survey was conducted with ACA and 12 m arrays at Band 6 towards 139 protoclusters from October 2021 to June 2024. Further details on the observational setup and data reduction are provided in [Liu et al. \(2024\)](#). Briefly, The ACA and TM2 combined dataset of this work yields an angular resolution of  $\sim 1.3''$ , and a typical rms noise level of  $\sim 5$  mJy beam<sup>-1</sup>. The flux calibration uncertainty is estimated at  $\sim 10\%$ . Four spectral windows (SPW 1-4), each with a bandwidth of 1.875 GHz, were centered at 217.918, 220.319, 231.370, and 233.520 GHz. The uniform spectral resolution of 976.56 kHz corresponds to a velocity resolution ( $\delta V$ ) of 1.2 km s<sup>-1</sup>, sufficient to spectrally resolve broad molecular lines.

### 3. Results

#### 3.1. Molecular Line Identifications

Spectroscopic data for  $\text{NH}_2\text{CHO}$  and its <sup>13</sup>C isotopolog ( $\text{NH}_2^{13}\text{CHO}$ ) were obtained from CDMS<sup>1</sup> (the Cologne Database for Molecular Spectroscopy, [Müller et al. 2001, 2005](#)), while data for  $\text{CH}_3\text{CONH}_2$  were adopted from [Ilyushin et al. \(2004\)](#). The spectral modeling was performed using GILDAS<sup>2</sup> (Grenoble Image and Line Data Analysis Software) to simulate the observed emission, with five parameters: source size, line width, velocity offset, rotational temperature, and column density. Of these, only the rotational temperature and column density were treated as free parameters. Source sizes were based on deconvolved continuum angular sizes; line widths were derived via Gaussian fitting; velocity offsets were calibrated using the  $\text{CH}_3\text{OH}$  line at 218440.063 MHz. Transitions heavily blended with intense lines from other species were excluded from the fitting. For partially blended transitions, multi-component Gaussian fitting was applied, and the contribution from overlapping species was estimated and subtracted using the best-fit synthetic spectra based on local thermodynamic equilibrium (LTE) modeling.

Although line intensities peak at the continuum center, strong absorption and line blending complicate the analysis. A detailed line-by-line inspection revealed that most  $\text{CH}_3\text{CONH}_2$

transitions are blended with other species near the continuum peak, while  $\text{NH}_2\text{CHO}$  transitions suffer from significant absorption against bright continuum emission. To improve line identification in such cases, spectra were extracted from offset positions (as shown in Fig. A.1 in the Appendix), where most of the lines exhibit Gaussian profiles and are relatively bright compared to other positions.

$\text{CH}_3\text{CONH}_2$  was considered confidently detected in ten HMCs (see Table 2), each showing at least five unblended transitions with signal-to-noise ratios (S/N)  $\geq 3\sigma$  that match the modeled rest frequencies and intensities. This criterion minimizes contamination from noise or line blending and ensures robust molecular identification. This constitutes the largest known sample of  $\text{CH}_3\text{CONH}_2$  detections in HMCs to date and forms the basis for our subsequent analysis. Fig. 1 presents representative spectra of  $\text{CH}_3\text{CONH}_2$ ,  $\text{NH}_2\text{CHO}$ , and  $\text{NH}_2^{13}\text{CHO}$  in I17175 MM2, highlighting clearly resolved or slightly blended transitions. Spectra for the other nine sources with  $\text{CH}_3\text{CONH}_2$  detections are provided in Fig. B.1. Tables C.1–C.10 list all detected lines for each amides in ten HMCs.

Although several other HMCs also exhibit emission features potentially attributable to  $\text{CH}_3\text{CONH}_2$ , it is insufficient to claim a secure detection of this species in these sources, as two or less unblended transitions are observed. Thus, the focus of this study is solely on the secure detection of  $\text{CH}_3\text{CONH}_2$ . Sources that lack conclusive evidence for the existence of this species will be discussed in Appendix D.

#### 3.2. Molecular Parameter Calculations

Column densities and excitation temperatures were derived using rotational diagrams for molecules with at least three unblended transitions spanning a broad energy range (Fig. 2). This method was applied to nine sources with  $\text{CH}_3\text{CONH}_2$  detections (excluding I18089) and to one source (I18089) with sufficient  $\text{NH}_2^{13}\text{CHO}$  transitions.

For  $\text{CH}_3\text{CONH}_2$  in I18089, the rotational diagram was not employed due to the limited energy range (117.7–136.6 K) of five detected transitions, which precludes a reliable fit. Instead, its column density was estimated from a single unblended line, assuming the excitation temperature derived from  $\text{NH}_2^{13}\text{CHO}$  in the same source. Similarly, for sources with fewer than three clean  $\text{NH}_2^{13}\text{CHO}$  transitions, column densities were estimated

<sup>1</sup> <https://cdms.astro.uni-koeln.de>

<sup>2</sup> <http://www.iram.fr/IRAMFR/GILDAS>



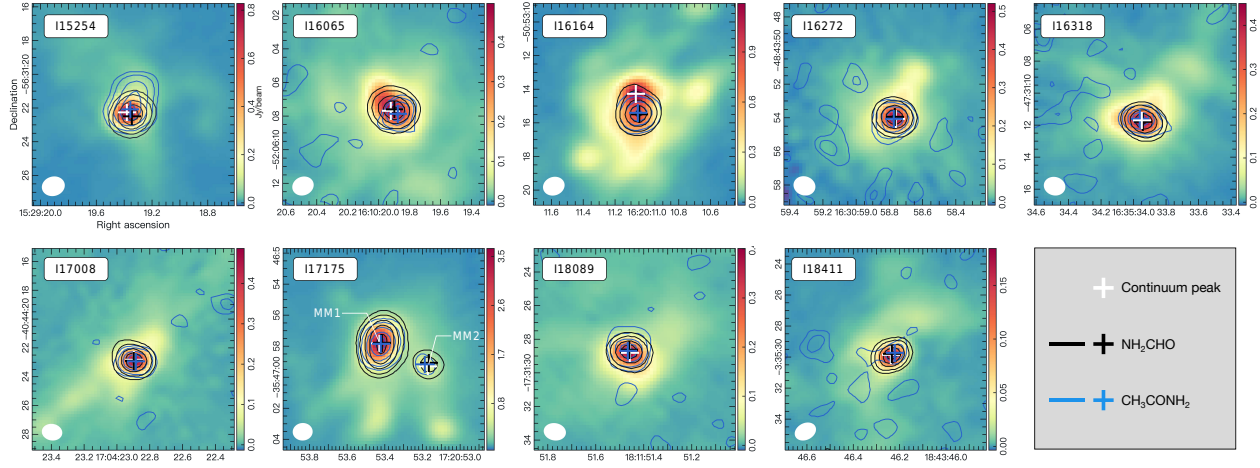


**Fig. 3.** Integrated emission maps of  $\text{NH}_2\text{CHO}$  (black) and  $\text{CH}_3\text{CONH}_2$  (blue), overlaid with 1.3 mm continuum emission. Contour levels are 10%, 20%, 40%, 60%, and 80% of the peak values. The solid ellipse in the bottom left corner indicates the synthesized beam for the continuum.

using individual lines and the excitation temperature obtained from  $\text{CH}_3\text{CONH}_2$ . Column densities ( $N$ ) were calculated under the assumptions of LTE and optically thin emission, following the standard rotational diagram formalism (Li et al. 2022):

$$N_l = \frac{8\pi\nu^2}{hc^3 A_{ul}} \frac{Q}{g_u} e^{E_u/kT_{\text{ex}}} \int T_{\text{mb}} dv, \quad (1)$$

where  $k$  is the Boltzmann constant,  $\nu$  the transition frequency,  $h$  the Planck constant,  $c$  the speed of light,  $A_{ul}$  the Einstein emission coefficient,  $g_u$  the upper level degeneracy, and  $E_u$  the upper-level energy. Due to optical thickness of  $\text{NH}_2\text{CHO}$  lines, their column densities were instead derived from the optically thin  $\text{NH}_2^{13}\text{CHO}$  isotopolog, scaled by the appropriate  $^{12}\text{C}/^{13}\text{C}$  ratio for each source. These ratios were calculated following the equation described by Yan et al. (2023) and are tabulated in Column 8 of Table 1. While this method effectively avoids opacity-related biases, several factors may introduce uncertainties into the observed  $^{12}\text{C}/^{13}\text{C}$  ratios. As noted by Yan et al. (2023), these include distance effects, beam size variations, excitation temperature mismatches, isotope-selective photodissociation, and chemical fractionation. Although the first three effects are likely minor, the latter two may be significant in regions with strong UV fields or non-equilibrium chemistry. For example, isotope-selective photodissociation may enhance the  $^{12}\text{C}/^{13}\text{C}$  ratio in photon-dominated regions (PDRs), whereas chemical fractionation could either increase or decrease the abundance of  $^{13}\text{C}$ -bearing species depending on formation pathways.

Table 2 summarizes the derived column densities and excitation temperatures, along with abundances relative to  $\text{CH}_3\text{OH}$ . The  $\text{CH}_3\text{OH}$  column densities were adopted from Qin et al. (2022). Abundances relative to  $\text{H}_2$  are not reported due to uncertainties in dust opacity.  $\text{CH}_3\text{CONH}_2$  column densities range from  $(2.5 \pm 0.9) \times 10^{14}$  to  $(1.5 \pm 0.6) \times 10^{16} \text{ cm}^{-2}$ , with excitation temperatures between 110 and 178 K.  $\text{NH}_2\text{CHO}$  exhibits consistently higher column densities, ranging from  $(1.1 \pm 0.1) \times 10^{15}$  to  $(6.9 \pm 0.4) \times 10^{16} \text{ cm}^{-2}$ , typically 3–9 times those of  $\text{CH}_3\text{CONH}_2$ .

### 3.3. Spatial distribution

The spatial distributions of  $\text{NH}_2\text{CHO}$  and  $\text{CH}_3\text{CONH}_2$  were analyzed using the Cube Analysis and Rendering Tool for Astronomy (CARTA; Comrie et al. 2021) to investigate their morphology and potential chemical link. Fig. 3 presents the integrated

intensity (moment-0) maps of both molecules overlaid on the 1.3 mm continuum emission. All selected transitions were individually checked to avoid contamination from line blending. Overall, amide emissions appear compact and generally coincide with the continuum peaks across all sources, except for I16164, where spatial offsets are observed. This deviation is consistent with the presence of an ultracompact  $\text{H II}$  region reported by (Zhang et al. 2023) and similar offsets for other COMs reported in Qin et al. (2022). In all HMCs,  $\text{CH}_3\text{CONH}_2$  and  $\text{NH}_2\text{CHO}$  show similar spatial distributions, supporting their chemical linkage.

## 4. Discussion

### 4.1. Detection and Distribution of $\text{CH}_3\text{CONH}_2$

$\text{CH}_3\text{CONH}_2$ , a key interstellar amide following  $\text{NH}_2\text{CHO}$ , has previously been detected in only a few individual sources. Based on unblended emission features, we report its detection in ten HMCs from the QUARKS sample, significantly increasing the number of known  $\text{CH}_3\text{CONH}_2$  emitters in the ISM (Fig. 4). This finding suggests that complex amides may be more widespread in star-forming regions than previously recognized, providing new observational constraints on their potential role in prebiotic chemistry.

### 4.2. Chemical links between $\text{NH}_2\text{CHO}$ and $\text{CH}_3\text{CONH}_2$

To explore potential chemical connections between  $\text{CH}_3\text{CONH}_2$  and  $\text{NH}_2\text{CHO}$ , their abundances were normalized to  $\text{CH}_3\text{OH}$ , a standard reference for COMs in the ISM. For our sources,  $\text{CH}_3\text{OH}$  column densities were adopted from Qin et al. (2022). For literature sources, values were adopted from Cernicharo et al. 2016, Bøgelund et al. 2018, Jørgensen et al. 2018, Bonfand et al. 2019, Ligterink et al. 2022, and Mininni et al. 2023, assuming a 20% uncertainty where not specified.

For comparison, we incorporated observational data from both high- and low-mass sources including Sgr B2(N2) (Belloche et al. 2017), G31.41+0.31 (Colzi et al. 2021), Orion KL (Cernicharo et al. 2016), IRAS 16293-2422B (Ligterink et al. 2018), NGC6334I MM1/MM2 (Ligterink et al. 2020), and Serpens SMM1-a (Ligterink et al. 2022), along with relevant chemical models (Garrod et al. 2022) and laboratory experimental result (Ligterink et al. 2018). While NGC6334I MM1/MM2 (Ligterink et al. 2020) correspond to the same

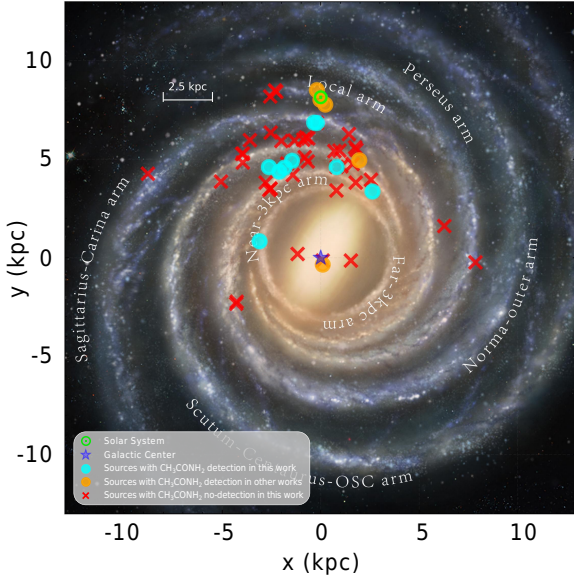


**Fig. 4.** Spatial distribution of  $\text{CH}_3\text{CONH}_2$ -detected sources projected onto a schematic top-down view of the Milky Way. Cyan symbols represent sources with  $\text{CH}_3\text{CONH}_2$  detections in this work, red symbols indicate sources where  $\text{CH}_3\text{CONH}_2$  was not detected, and orange symbols denote previously reported detections from other studies. Notably, IRAS 17175 MM1/MM2 (this work) and NGC 6334I MM1/MM2 (Ligterink et al. 2020) refer to the same HMCs and are therefore shown exclusively with cyan symbols.

physical sources as I17175 MM1/MM2 in our sample, the  $\text{CH}_3\text{CONH}_2$  column densities derived in this work are lower, likely due to more offset spectral extraction positions. Despite this, the  $\text{NH}_2\text{CHO}/\text{CH}_3\text{CONH}_2$  abundance ratios agree well between the two studies (4.5 for MM1 and 3.0 for MM2 in our work vs. 12.3 for MM1 and 3.1 for MM2 in Ligterink et al. (2020)), supporting the reliability of our detections. Therefore, values from NGC 6334I were excluded from further statistical analysis to avoid duplication.

As shown in Fig. 5a,  $\text{CH}_3\text{CONH}_2$  and  $\text{NH}_2\text{CHO}$  abundances exhibit a strong positive correlation, with a best-fit power law:

$$X_{\text{CH}_3\text{OH}}(\text{CH}_3\text{CONH}_2) = (0.08 \pm 0.07) \times X_{\text{CH}_3\text{OH}}(\text{NH}_2\text{CHO})^{(0.86 \pm 0.15)} \quad (2)$$

This trend indicates a potential chemical link for the two species across diverse astrophysical environments.

The  $\text{NH}_2\text{CHO}/\text{CH}_3\text{CONH}_2$  ratios in our sample range from 2.9 to 8.9, with an average of  $\sim 5.6$  and a standard deviation of  $\pm 1.8$ , exhibiting relatively small variation across sources (Fig. 4b). These values are broadly consistent with those reported for Orion KL and IRAS 16293-2422B, although they lie near the lower end of our observed range. G31.41+0.31, with a ratio of  $\sim 2$ , is significantly lower than our sample average ( $\sim 5.6$ ), while higher ratios have been reported for Sgr B2(N2) ( $\sim 25$ ; Belloche et al. 2017) and SMM1-a ( $\sim 18$ ; Ligterink et al. 2022), exceeding average of this work by factors of  $\sim 4.5$ , and  $\sim 3.2$ , respectively. The observed discrepancies may arise from multiple factors. While uncertainties in excitation temperatures significantly affect the derived column densities, other contributors include optical depth, line blending, spatial structure, and assumptions of LTE. In this work, potential limitations involve the use of  $^{13}\text{C}$  isotopologs of  $\text{NH}_2\text{CHO}$  to correct for optical depth effects in its emission lines. Additionally, the adopted assumption of uni-

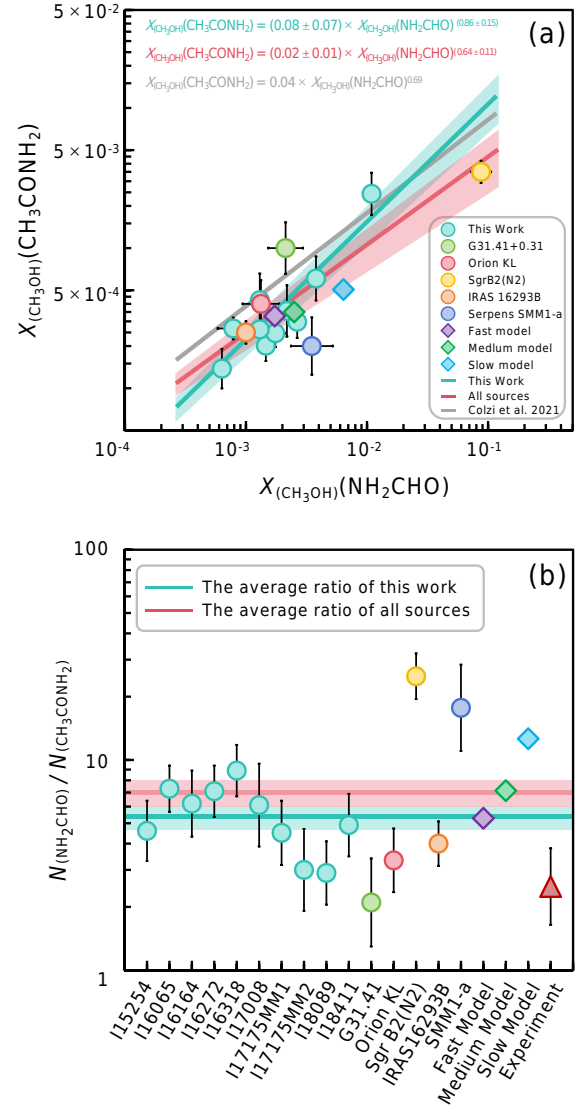


**Fig. 5.** a)  $X_{\text{CH}_3\text{OH}}(\text{CH}_3\text{CONH}_2)$  as a function of  $X_{\text{CH}_3\text{OH}}(\text{NH}_2\text{CHO})$ . The cyan line and shaded region denote the power-law fit and its uncertainty derived in this work; the red line and shaded region represent the fit and its uncertainty obtained by combining our sources with previous studies; and the gray line shows the fit from Colzi et al. (2021). Symbols and colors correspond to different sources, as shown in the legend. b)  $\text{NH}_2\text{CHO}/\text{CH}_3\text{CONH}_2$  ratios. Ratios for this work are indicated in cyan, while those from previous studies are shown in different colors. The cyan line and shaded region represent the mean ratio and its uncertainty for our data, and the red solid line and shaded region represent the combined sample ratio.

form source-filling emission for  $\text{CH}_3\text{CONH}_2$  may lead to systematic uncertainties. Nevertheless, it is noteworthy that even with these discrepancies, the reported ratios from these works still fall within the same order of magnitude as our study. Given the sensitivity of COM abundances to both temperature and evolutionary stage (Garrod 2013; Garrod et al. 2022), the observed stability suggests that  $\text{NH}_2\text{CHO}$  and  $\text{CH}_3\text{CONH}_2$  likely form under similar physical and chemical conditions (Quénard et al. 2018; Belloche et al. 2020).

### 4.3. Formation Pathways of $\text{CH}_3\text{CONH}_2$

Several formation pathways have been proposed for  $\text{CH}_3\text{CONH}_2$ . Hollis et al. (2006) suggested a gas-phase route involving the addition of a  $\text{CH}_2$  radical to  $\text{NH}_2\text{CHO}$ . However, theoretical studies by Quan & Herbst (2007) indicate that this reaction requires a spin-flip transition of  $\text{CH}_2$  from the triplet to singlet state, with an energy barrier exceeding 1000 K—rendering it unlikely under typical interstellar conditions. Other proposed gas-phase reactions, such as radiative association between  $\text{NH}_2\text{CHO}$  and  $\text{CH}_3^+$  (Quan & Herbst 2007), predict  $\text{CH}_3\text{CONH}_2$  abundances ( $\sim 10^{-15}$ ) far below observed levels.

In contrast, grain-surface chemistry offers a more viable formation mechanism. Agarwal et al. (1985) proposed that  $\text{CH}_3\text{CONH}_2$  can form via the reaction between the  $\text{CH}_3$  radical and the  $\text{NH}_2\text{CO}$  intermediate—a key species linking  $\text{NH}_2\text{CHO}$  and  $\text{CH}_3\text{CONH}_2$ . The  $\text{NH}_2\text{CO}$  radical may arise through hydrogen abstraction from  $\text{NH}_2\text{CHO}$ , radical addition of  $\text{NH}_2$  and CO, or hydrogenation of  $\text{HNCO}$  (Belloche et al. 2017, 2019; Garrod et al. 2022). Belloche et al. (2017) predicted an  $\text{NH}_2\text{CHO}/\text{CH}_3\text{CONH}_2$  ratio of  $\sim 15$  assuming only the hydrogen abstraction route. In contrast, Garrod et al. (2022) considered multiple grain-surface formation pathways for  $\text{CH}_3\text{CONH}_2$ , including: (i)  $\text{CH}_3 + \text{NH}_2\text{CO} \rightarrow \text{CH}_3\text{CONH}_2$ , (ii) H-abstraction from  $\text{NH}_2\text{CHO}$  forming  $\text{NH}_2\text{CO}$ , followed by  $\text{CH}_3$  addition, and (iii) hydrogenation of  $\text{HNCO}$  leading to  $\text{NH}_2\text{CO}$  intermediates. These mechanisms all involve  $\text{NH}_2\text{CO}$  as a key radical intermediate, thereby establishing a direct chemical connection between  $\text{NH}_2\text{CHO}$  and  $\text{CH}_3\text{CONH}_2$ . Our observed abundance ratios (2.9–8.9) align with Garrod et al.’s predicted range (5–13), providing strong support for a linked formation pathway through grain-surface chemistry.

The strong abundance correlation between  $\text{NH}_2\text{CHO}$  and  $\text{CH}_3\text{CONH}_2$  may also reflect their co-formation on dust grains, followed by thermal desorption under similar physical conditions—paralleling trends observed for  $\text{HNCO}$  and  $\text{NH}_2\text{CHO}$  (Quénard et al. 2018). Laboratory data further support this view: Ligterink et al. (2018) measured similar desorption temperatures for  $\text{CH}_3\text{CONH}_2$  (219 K) and  $\text{NH}_2\text{CHO}$  (210 K), while ice mantle simulations yielded a desorption ratio of  $\text{NH}_2\text{CHO}/\text{CH}_3\text{CONH}_2 \sim 2.5^{+1.3}_{-1.2}$ , comparable to our average observed value of 5.6.

Taken together, these findings strongly favor a formation scenario in which  $\text{CH}_3\text{CONH}_2$  is synthesized via grain-surface chemistry closely linked to  $\text{NH}_2\text{CHO}$ , followed by co-desorption in star-forming regions. Nonetheless, additional laboratory, observational, and modeling efforts are required to fully constrain the dominant formation routes.

## 5. Conclusions

We present the first systematic survey of acetamide ( $\text{CH}_3\text{CONH}_2$ ), a key interstellar amide, in hot molecular cores (HMCs) using ALMA-QUARKS data. The joint detections of formamide ( $\text{NH}_2\text{CHO}$ ) enable a comparative analysis of their abundance correlation and formation chemistry. Our main findings are as follows:

- Both  $\text{NH}_2\text{CHO}$  and  $\text{CH}_3\text{CONH}_2$  were detected in ten HMCs, increasing the number of known  $\text{CH}_3\text{CONH}_2$  sources to 17 and providing the most extensive sample to date for this molecule.
- $\text{CH}_3\text{CONH}_2$  column densities, derived via rotational diagram analysis, range from  $(2.5 \pm 0.9) \times 10^{14}$  to  $(1.5 \pm 0.6) \times$

$10^{16} \text{ cm}^{-2}$ .  $\text{NH}_2\text{CHO}$  column densities, estimated from optically thin  $^{13}\text{C}$  isotopologs, range from  $(1.1 \pm 0.1) \times 10^{15}$  to  $(6.9 \pm 0.4) \times 10^{16} \text{ cm}^{-2}$ —typically 3–9 times those of  $\text{CH}_3\text{CONH}_2$ .

- The  $\text{NH}_2\text{CHO}/\text{CH}_3\text{CONH}_2$  ratio remains nearly constant ( $\sim 5.6$  on average) across all detected sources. A strong correlation between the two species follows a power-law relation, supporting a chemically linked formation pathway, likely dominated by grain-surface reactions.

These results provide compelling evidence for the presence of complex amide molecules in star-forming regions. The inferred chemical association between  $\text{NH}_2\text{CHO}$  and  $\text{CH}_3\text{CONH}_2$  highlights the potential role of surface chemistry in assembling peptide-relevant structures prior to planetary formation. The eventual incorporation of such molecules into nascent planetary systems—via cometary or meteoritic delivery—may have contributed essential building blocks for prebiotic chemistry on early Earth and potentially elsewhere. Continued laboratory, observational, and modeling efforts are required to further constrain the dominant formation routes and the broader astrochemical role of interstellar amides.

## 6. Data availability

The derived data underlying this article are available in the article and in its online supplementary material on [zenodo](#).

**Acknowledgements.** This work makes use of the following ALMA data: ADS/JAO.ALMA#2021.1.00095.S. ALMA is a partnership of ESO (representing its member states), NSF (USA), and NINS (Japan), together with NRC (Canada), MOST and ASIAA (Taiwan, China), and KASI (Republic of Korea), in cooperation with the Republic of Chile. The Joint ALMA Observatory is operated by ESO, AUI/NRAO, and NAOJ. We sincerely thank Prof. Shengli Qin and Dongting Yang (Yunnan University) for their assistance with the data processing. This work was supported by the Fundamental Research Funds for the Central Universities (Grant Nos. 2024CDJGF-025 and 2023CDJXY-045), Chongqing Municipal Natural Science Foundation General Program (Grant No. cstc2021jcyj-msxmX0867), National Natural Science Foundation of China (Grant No. 12103010), and Strategic Priority Research Program of the Chinese Academy of Sciences (Grant No. XDB0800303).

## References

- Agarwal, V. K., Schutte, W., Greenberg, J. M., et al. 1985, *Origins of Life*, 16, 21
- Belloche, A., Garrod, R. T., Müller, H. S. P., et al. 2019, *A&A*, 628, A10
- Belloche, A., Maury, A. J., Maret, S., et al. 2020, *A&A*, 635, A198
- Belloche, A., Meshcheryakov, A. A., Garrod, R. T., et al. 2017, *A&A*, 601, A49
- Bøgelund, E. G., McGuire, B. A., Ligterink, N. F. W., et al. 2018, *A&A*, 615, A88
- Bonfand, M., Belloche, A., Garrod, R. T., et al. 2019, *A&A*, 628, A27
- Cernicharo, J., Kiesel, Z., Tercero, B., et al. 2016, *A&A*, 587, L4
- Chyba, C. & Sagan, C. 1992, *Nature*, 355, 125
- Chyba, C. F., Thomas, P. J., Brookshaw, L., & Sagan, C. 1990, *Science*, 249, 366
- Colzi, L., Rivilla, V. M., Beltrán, M. T., et al. 2021, *A&A*, 653, A129
- Comrie, A., Wang, K.-S., Hsu, S.-C., et al. 2021, *CARTA: The Cube Analysis and Rendering Tool for Astronomy*
- Garrod, R. T. 2013, *ApJ*, 765, 60
- Garrod, R. T., Jin, M., Matis, K. A., et al. 2022, *ApJS*, 259, 1
- Halfen, D. T., Ilyushin, V., & Ziurys, L. M. 2011, *ApJ*, 743, 60
- Hollis, J. M., Lovas, F. J., Remijan, A. J., et al. 2006, *ApJ*, 643, L25
- Ilyushin, V. V., Alekseev, E. A., Dyubko, S. F., Kleiner, I., & Hougen, J. T. 2004, *Journal of Molecular Spectroscopy*, 227, 115
- Jørgensen, J. K., Müller, H. S. P., Calcutt, H., et al. 2018, *A&A*, 620, A170
- Li, Y., Wang, J., Li, J., Liu, S., & Luo, Q. 2022, *MNRAS*, 512, 4934
- Ligterink, N. F. W., Ahmadi, A., Luitel, B., et al. 2022, *ACS Earth and Space Chemistry*, 6, 455
- Ligterink, N. F. W., Coutens, A., Kofman, V., et al. 2017, *MNRAS*, 469, 2219
- Ligterink, N. F. W., El-Abd, S. J., Brogan, C. L., et al. 2020, *ApJ*, 901, 37

- Ligterink, N. F. W., Terwisscha van Scheltinga, J., Taquet, V., et al. 2018, *MNRAS*, 480, 3628
- Liu, T., Evans, N. J., Kim, K.-T., et al. 2020, *MNRAS*, 496, 2790
- Liu, X., Liu, T., Shen, Z., et al. 2022, *ApJS*, 263, 13
- Liu, X., Liu, T., Zhu, L., et al. 2024, *Research in Astronomy and Astrophysics*, 24, 025009
- López-Sepulcre, A., Balucani, N., Ceccarelli, C., et al. 2019, *ACS Earth and Space Chemistry*, 3, 2122
- Mininni, C., Beltrán, M. T., Colzi, L., et al. 2023, *A&A*, 677, A15
- Müller, H. S. P., Schlöder, F., Stutzki, J., & Winnewisser, G. 2005, *Journal of Molecular Structure*, 742, 215
- Müller, H. S. P., Thorwirth, S., Roth, D. A., & Winnewisser, G. 2001, *A&A*, 370, L49
- Patel, B. H., Percivalle, C., Ritson, D. J., Duffy, C. D., & Sutherland, J. D. 2015, *Nature Chemistry*, 7, 301
- Pauling, L., Corey, R. B., & Branson, H. R. 1951, *Proceedings of the National Academy of Science*, 37, 205
- Pearce, B. K. D., Tupper, A. S., Pudritz, R. E., & Higgs, P. G. 2018, *Astrobiology*, 18, 343
- Qin, S.-L., Liu, T., Liu, X., et al. 2022, *MNRAS*, 511, 3463
- Quan, D. & Herbst, E. 2007, *A&A*, 474, 521
- Quénard, D., Jiménez-Serra, I., Viti, S., Holdship, J., & Coutens, A. 2018, *MNRAS*, 474, 2796
- Xu, X., Wang, J., Gou, Q., et al. 2025, *PASJ*, 77, 307
- Yan, Y. T., Henkel, C., Kobayashi, C., et al. 2023, *A&A*, 670, A98
- Zeng, S., Rivilla, V. M., Jiménez-Serra, I., et al. 2023, *MNRAS*, 523, 1448
- Zhang, C., Zhu, F.-Y., Liu, T., et al. 2023, *MNRAS*, 520, 3245
- Zheng, S., Li, J., Wang, J., et al. 2024, *ApJ*, 961, 58



## Appendix A: Spectral Extraction positions.

To minimize the effects of absorption and line blending, we extracted spectra at offset positions from the continuum peaks for further analysis. The extraction positions for each source are shown in Fig. A.1, where they are marked by white points.

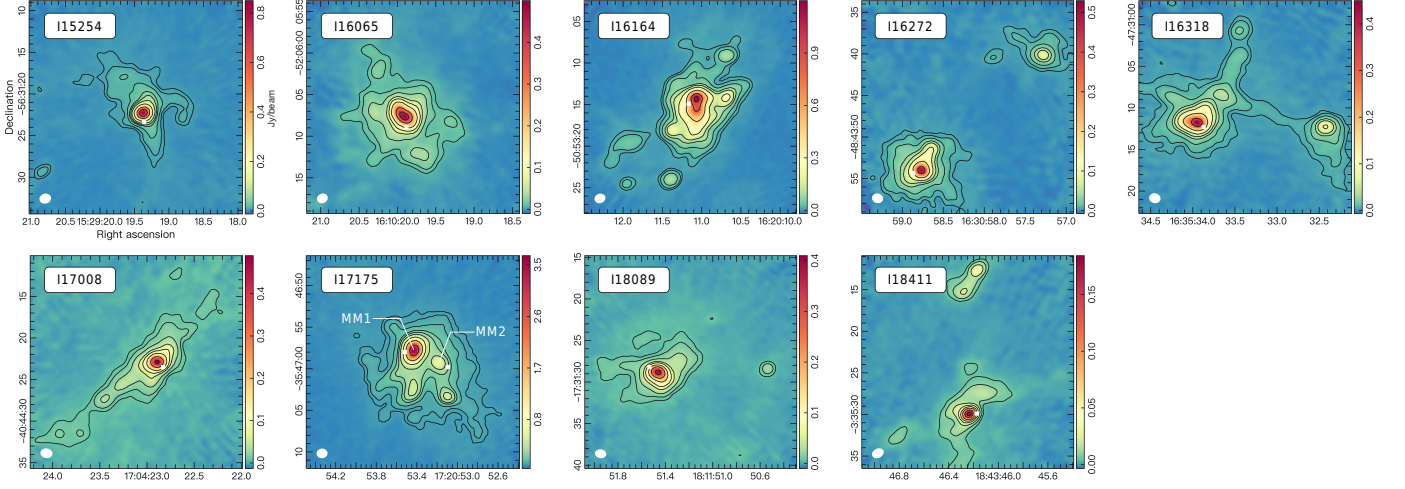


**Fig. A.1.** 1.3 mm continuum image of I15254, I16065, I16164, I16272, I16318, I17008, I17175, I18089, and I18411 obtained with ALMA band 6. The background shows the continuum emission of each source. Contour levels are drawn at  $(3, 5, 10, 20, 30, 50, 100, 200) \times \sigma$ , where  $\sigma$  is the rms noise level. The  $1\sigma$  values of I15254, I16065, I16164, I16272, I16318, I17008, I17175, I18089, and I18411 are 1.92, 2.75, 4.13, 1.75, 1.51, 2.80, 6.90, 2.60, 2.80 mJy beam<sup>-1</sup>, respectively. The synthetic beam for continuum is indicated in the bottom left corner by the ellipse. The spectral extraction positions are indicated with a white point.

## Appendix B: The identified spectral lines of amide molecules.

The emissions of  $\text{CH}_3\text{CONH}_2$ ,  $\text{NH}_2\text{CHO}$ , and  $\text{NH}_2^{13}\text{CHO}$  are detected in ten sources. Fig. B.1 show the detected transitions of these amide molecules, which are not covered in the Fig. 1, for all hot cores.

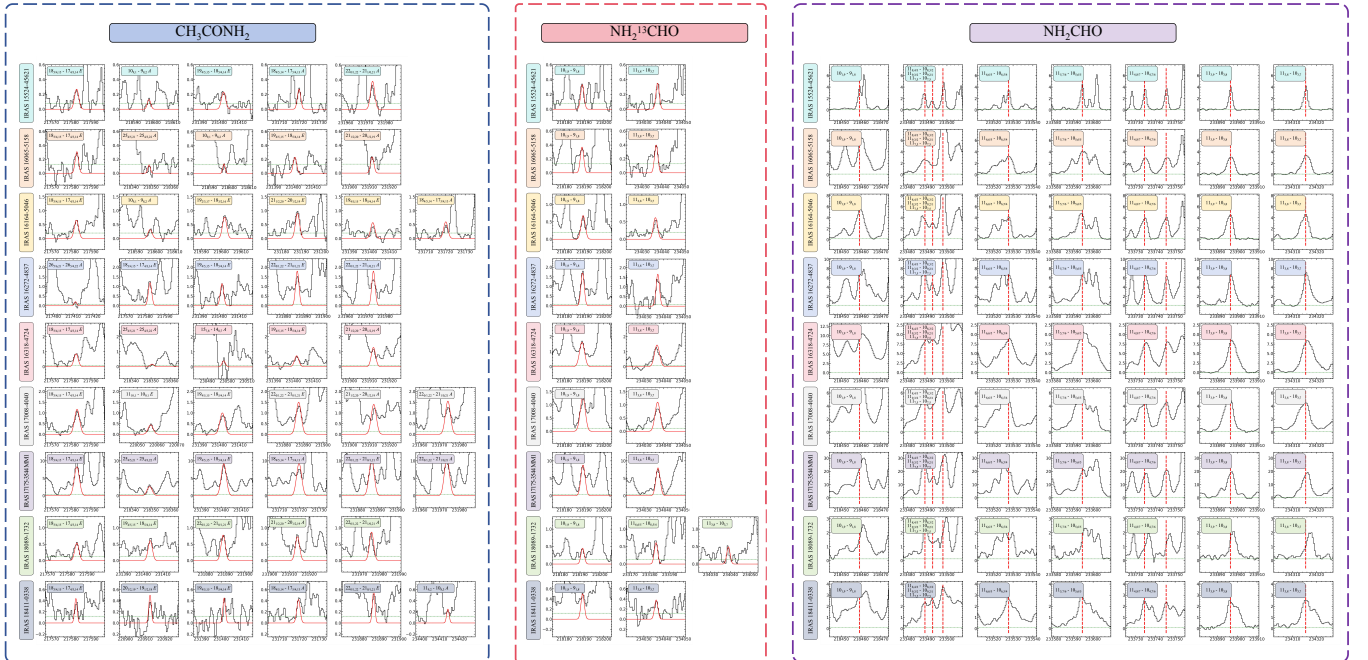


**Fig. B.1.** Observed (black) and modeled (red) spectra of  $\text{CH}_3\text{CONH}_2$ ,  $\text{NH}_2\text{CHO}$ , and  $\text{NH}_2^{13}\text{CHO}$  in nine HMCs. Clearly resolved or slightly blended transitions are shown. Green dashed lines mark the  $3\sigma$  noise level. No modeled spectrum is shown for  $\text{NH}_2\text{CHO}$  due to optical thickness. Red dashed lines indicate the rest frequencies of  $\text{NH}_2\text{CHO}$  transitions. The y-axis shows the line intensity in Kelvin, and the x-axis shows the frequency in MHz.



## Appendix C: Summary of detected molecular lines.

This appendix presents the statistics of detected lines in our observations. Tables C.1–C.10, only available at the [zenodo](#), compile all detected line information for each amide species across the ten HMCs. These data provide essential constraints for the derivation of column densities and excitation temperatures.

## Appendix D: The upper limits of column density for $\text{CH}_3\text{CONH}_2$ in undetected sources.

For the 42 sources where  $\text{CH}_3\text{CONH}_2$  was not detected,  $3\sigma$  upper limits for its column density has been derived. Fig D.1(a) compares these upper limits with the derived column densities in the 10 detections. The upper limits generally fall within an order of magnitude of the detected values, suggesting that sensitivity limitations may account for many of the non-detections, rather than a true absence of  $\text{CH}_3\text{CONH}_2$ . To further explore this, the relationship between  $\text{CH}_3\text{CONH}_2/\text{CH}_3\text{OH}$  ratios and  $\text{CH}_3\text{OH}$  column densities have been examined (Fig D.1(b)). All ten  $\text{CH}_3\text{CONH}_2$ -detected sources exhibit higher  $\text{CH}_3\text{OH}$  column densities, supporting the idea that  $\text{CH}_3\text{CONH}_2$  is more likely to be detected in chemically rich environments. Nonetheless, 6 non-detected sources with  $\text{CH}_3\text{OH}$  column densities  $> 4 \times 10^{18} \text{ cm}^{-2}$ , show no  $\text{CH}_3\text{CONH}_2$  detection, suggesting that  $\text{CH}_3\text{OH}$  abundance alone is not a sufficient predictor. These results emphasize the need for higher-sensitivity observations to better constrain the prevalence and formation conditions of interstellar acetamide.

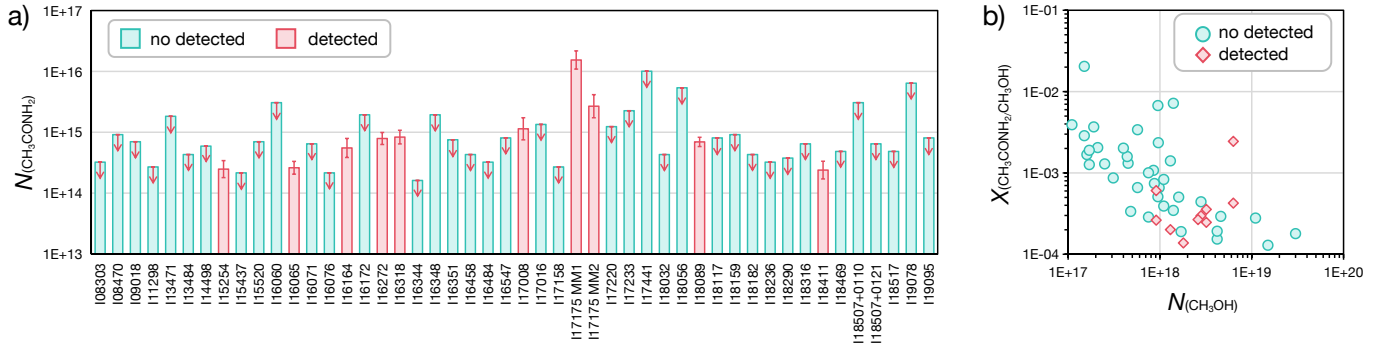


**Fig. D.1.** (a) Derived column densities (10 sources with  $\text{CH}_3\text{CONH}_2$  detections, indicated in red) or upper limits (42 sources without  $\text{CH}_3\text{CONH}_2$  detections, indicated in cyan) among all sources. (b) The relationship between the  $\text{CH}_3\text{CONH}_2/\text{CH}_3\text{OH}$  and  $\text{CH}_3\text{OH}$  column densities.